ACS NANO

www.acsnano.org

Article

Confining Metastable Wurtzite HgTe for Infrared Optoelectronics

Kseniia A. Sergeeva,[††] Arsenii S. Portniagin,[††] Dario Mastrippolito, Clement Gureghian, Antoine Hage, Dries De Pesseroey, Marco Paye, Erwan Bossavit, Aleksandr A. Sergeev, Zhuo Li, Albin Colle, Céline Rivaux, Sandrine Ithurria, Peter Reiss, Gilles Patriarche, Xiaoyan Zhong, Jing Li, Stefan Klotz, Benoit Baptiste, Debora Pierucci, Francesco Capitani, Christophe Delerue, Andrey L. Rogach,* and Emmanuel Lhuillier*

Cite This: *ACS Nano* 2026, 20, 10686−10695

Read Online

ACCESS | Metrics & More | Article Recommendations | Supporting Information

ABSTRACT: Mercury telluride (HgTe) nanocrystals are cornerstone materials for infrared optoelectronics, yet all previously reported forms of HgTe have crystallized in the zinc blende phase. Here, we develop a comprehensive cation exchange route to access metastable wurtzite (WZ) HgTe in both spherical and nanorod morphologies. Structural and spectroscopic characterizations show that WZ HgTe NCs retain the strong confinement tunability of their optical properties while introducing non-cubic lattice and distinct electronic topology. *Ab initio* modeling reveals that bulk WZ HgTe is a Dirac semimetal, whereas quantum confinement opens a direct gap that enables bright short-wave infrared emission. High-pressure studies demonstrate an irreversible WZ-to-zinc blende phase transition, consistent with its metastable nature, while the WZ phase remains stable at cryogenic temperatures. Electrically driven light-emitting diodes based on WZ HgTe nanorods exhibit superior electroluminescence beyond 2 μm, establishing a platform bridging topological semimetals and confined infrared emitters.

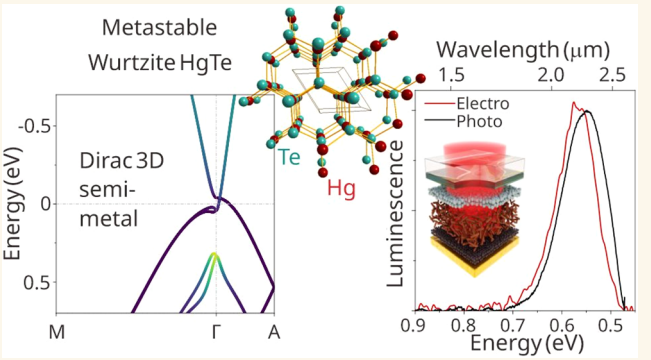

KEYWORDS: *HgTe, wurtzite, nanocrystals, Dirac 3D semimetal, pressure-induced phase transition, infrared light-emitting diode*

INTRODUCTION

Among semiconductor materials, mercury telluride (HgTe) stands out for its exceptionally broad spectral tunability across the entire infrared (IR) range, from the near-IR[1,2] to the terahertz region.[3] Bulk HgTe is a semimetal[4] with an inverted band structure,[5−7] a property that enables its application in long-wavelength infrared optoelectronics. Furthermore, its band gap can be readily widened either by alloying with Cd to form HgCdTe[4] or through quantum confinement effect.[8] The alloyed material has been extensively used for weak-photon-energy detection[9,10] and successfully commercialized.

Chemically synthesized colloidal HgTe nanocrystals (NCs) have emerged as an appealing alternative to epitaxially grown materials thanks to their infrared absorption, air stability, and exceptionally broad spectral tunability governed by the quantum confinement effect.[8] These properties motivated investigations into the electronic structure of HgTe NCs, which, however, remains only partially understood.[11−14] Moreover, the interest in HgTe has been further stimulated by the first experimental demonstration of a topological insulator based on this material.[15,16]

Until very recently, all reported HgTe materials under ambient conditions have been found to crystallize in the cubic zinc blende (ZB) phase.[17] This behavior contrasts with most other NCs from the II−VI binary semiconductor family, which can adopt either ZB or wurtzite (WZ) structures, both attainable through adjustments in ligand chemistry[18,19] or synthesis temperature.[20] In the case of CdTe, for example, the band gaps of these two crystal phases are well known and differ by a few tens of meV.[21] For a wide-band gap material (≈1.7 eV), such band gap variation would have little impact,[22] but for narrow-band gap HgTe NCs, a similar structural change could lead to dramatic renormalization of the electronic structure. This possible phase transition is of significant interest: compared to ZB, the valence band states of WZ NCs are less degenerate due to the splitting of the $1S_{3/2}$ hole level,[23] which can suppress Auger recombination and render WZ-based materials more promising for light-emitting applications.

Received: January 25, 2026
Revised: March 14, 2026
Accepted: March 16, 2026
Published: March 24, 2026

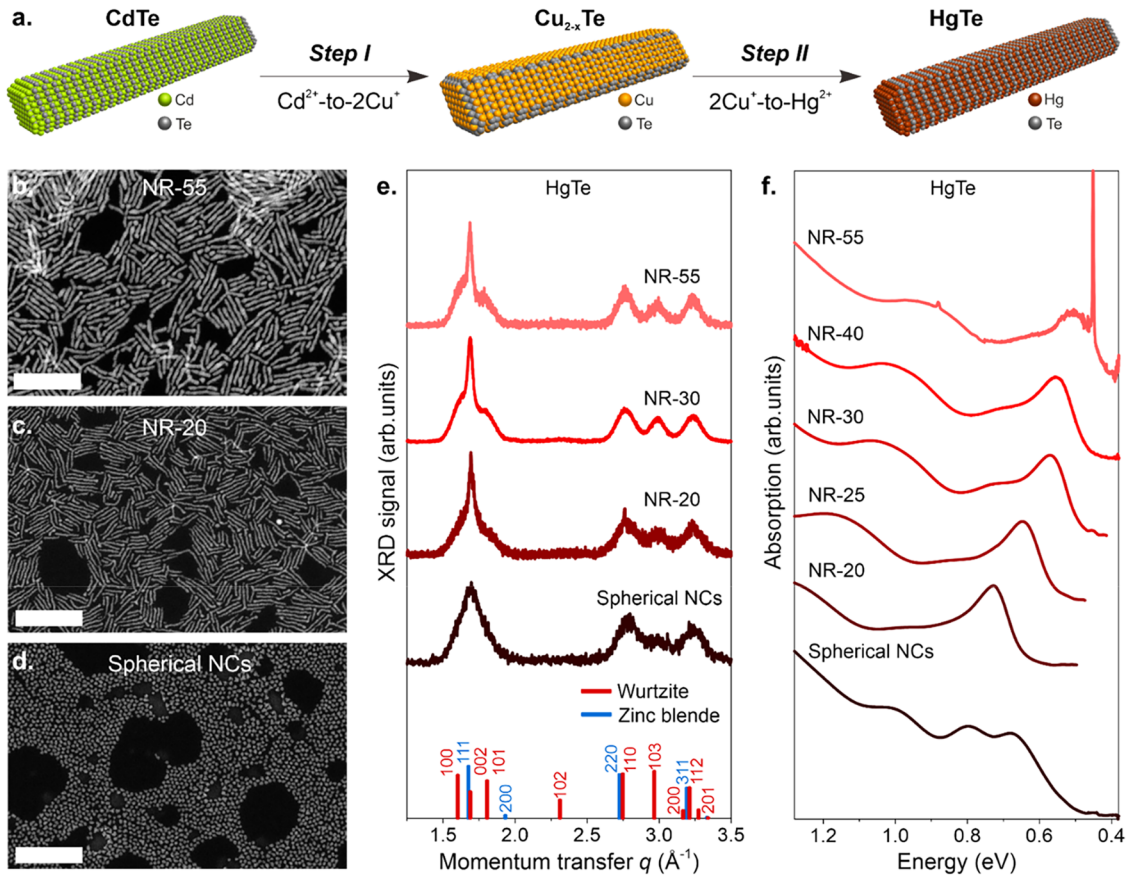

Figure 1. Formation of WZ HgTe NCs. (a) Schematic of the two-step Cd−Cu−Hg cation exchange process leading to the formation of WZ HgTe NRs. The same general procedure was used to obtain spherical WZ HgTe NCs. (b−d) Low-resolution TEM images of the elongated and spherical HgTe NCs. Scale bars are 50 nm. (e) XRD patterns of HgTe NCs recorded under ambient conditions. The presence of a feature at $q \approx 3$ Å^{-1} highlights wurtzite as the dominant crystalline phase. The reference XRD pattern for WZ HgTe does not exist, and instead, it was calculated for bulk CdTe (as shown by red bars). The reference pattern for ZB corresponds to bulk HgTe and is shown by blue bars. (f) Absorption spectra of HgTe NCs with various dimensions (both spherical and NRs).

Consequently, substantial efforts have been devoted to controlling the dimensions and morphology of HgTe NCs to finely tune their electronic and optical properties.

In this regard, anisotropic nonspherical NCs have become an active focus of research, enabling the formation of one-dimensional nanorods (NRs)[24,25] and two-dimensional nanoplatelets.[26,27] Nevertheless, direct synthesis methods based on hot injection are not able to produce uniformly shaped HgTe NCs adopting the WZ structure. Recently, Portniagin et al.[28] identified a cation exchange route enabling the growth of WZ HgTe NRs with a narrow size distribution inherited from the parent CdTe NR ensemble. This discovery opens a series of fundamental questions regarding the nature of this material phase for HgTe. The first concerns whether its band gap is trivial or topological. The second relates to its thermodynamic stability, as the phase diagram and temperature- or pressure-dependent optical properties of WZ HgTe are naturally unknown and, to date, have been established only for the ZB phase.[29,30]

In this work, we addressed these questions by developing an advanced cation exchange strategy that yields WZ HgTe NCs in both spherical and NR shapes. We determine, for the first time, the electronic structure of WZ HgTe NCs and define their pressure−temperature stability limits. Moreover, we demonstrate their potential for optoelectronic applications by realizing light-emitting diodes (LEDs) with strong electroluminescence in the extended short-wave IR range.

RESULTS AND DISCUSSION

Synthesis of WZ HgTe NCs

To obtain WZ HgTe NCs of spherical and NR shape, we have implemented a two-step cation exchange strategy,[28] starting with WZ CdTe NCs and followed by Cd-to-Cu and Cu-to-Hg cation exchange steps (Figure 1a). An intermediate Cd-to-Cu step is necessary here to attain complete conversion into HgTe, as direct Cd-to-Hg exchange retards at the very early stages[31,32] and does not allow the WZ HgTe phase to be formed. Importantly, both cation exchange steps have been thoroughly revised to provide Cd and Cu residue-free HgTe NCs with long-term colloidal stability and a reduced number of defects in the final material. Prior to cation exchange, the initial CdTe NCs were treated with a thiol/amine mixture to replace phosphonate ligands, which acted as the main source of Cd impurities and were not optimal stabilizers for copper chalcogenides (Figure S1).[33] In the first Cu-to-Cd cation exchange step, we employed an alternative copper precursor (Cu(I) oleate) to enhance colloidal stability in nonpolar solvents, yielding $Cu_{2-x}Te$ NCs with significantly reduced Cd content and minimized aggregation (Figure S2). In the second Cu-to-Hg cation exchange step, we systematically compared

https://doi.org/10.1021/acsnano.6c01515
ACS Nano 2026, 20, 10686−10695

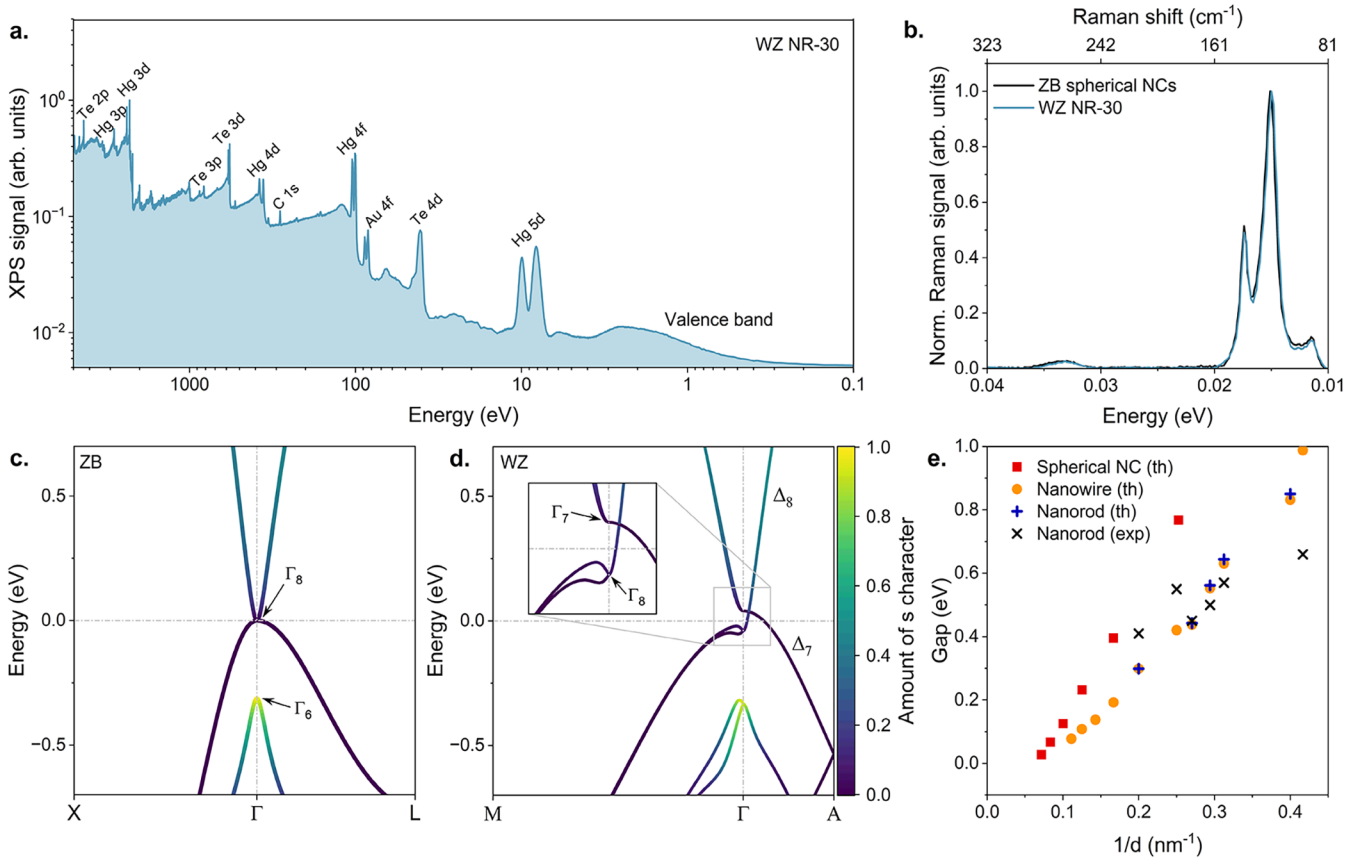

Figure 2. Electronic structure of WZ HgTe. (a) Broad range electronic spectrum of WZ HgTe NR-30 highlighting the core levels and valence band, obtained using the hard X-ray Cr source at 5414.8 eV. The spectra acquired using soft X-ray (1486.6 eV) are provided in Figure S14. (b) Raman spectra showing the lattice vibrations of WZ HgTe NR-30 and ZB HgTe spherical NCs of similar diameter. (c) Tight binding electronic structure of bulk ZB HgTe. The scale depicts the s character of the band. The zero of energy corresponds to the Fermi level. (d) Tight binding electronic structure of bulk WZ HgTe. The scale depicts the s character of the band. The inset in (d) shows band structure details including a 3D Dirac point along the Γ-A direction (along k_z). (e) Energy gap of spherical NCs (red squares), cylindrical nanowires of infinite length (orange dots), and nanorods (blue plus markers) of finite diameter and length (values taken from Table S1 as determined by electronic microscopy) calculated in tight binding method, compared to the optical gap defined for nanorods experimentally (black crosses).

Hg precursors with $-Cl_2$, $-NH_2$, −COOH, and −SH coordinating groups and found that Hg-thiolate precursors preserve NC size and morphology while further suppressing residual Cu content (Figures S3−S5). As a result, our optimized two-step cation exchange protocol allows us to obtain HgTe NCs with <1 atom % Cu and no detectable Cd, as confirmed by inductively coupled plasma optical emission spectrometry and energy-dispersive X-ray spectroscopy in Figure S6. Moreover, by altering the reactivity and the amount of tellurium precursor introduced into the reaction mixture, one can obtain HgTe NCs of spherical or NR shape (Figure 1b−d). From here on, we will denote the HgTe NR samples according to their respective length, e.g., NR-20 has length and diameter of 23 ± 3 and 2.4 ± 0.2 nm, respectively (all the samples are summarized in Table S1 and Figure S7).

X-ray diffraction (XRD) analysis performed under ambient conditions confirms that both spherical and NR-shaped HgTe NCs adopt the unusual WZ phase (Figure 1e), enabling the study of shape-dependent effects on the stability and optical properties of the hexagonal phase of HgTe. The growth of HgTe NRs along the [001] crystallographic axis (*c*-axis) leads to a narrowing of the XRD peak at q = 1.7 $Å^{-1}$ corresponding to the (002) plane, which becomes clearly noticeable when compared with that of spherical HgTe NCs that exhibit no preferred growth direction. The XRD data also confirm that the structural features of CdTe are inherited by HgTe NCs (Figure S8). A clear improvement in the content of the WZ HgTe phase is observed with the elongation of the NRs, reaching up to 90 ± 3% for the NR-55 sample, contrary to 70 ± 3% for spherical NCs.

The lattice parameters of the corresponding CdTe and HgTe NCs differ within the margins of experimental error, with the unit cell volume of HgTe being slightly smaller than that of CdTe (Figure S9 and Table S2). The average lattice parameters of the initial CdTe NCs are in good agreement with those of the bulk material, confirming that the NC lattice is not under significant strain. The unit cell volume increases systematically with the elongation of the NRs, indicating that the structure remains uncompressed under ambient conditions. Geometric phase analysis further demonstrates that strains in the NRs are distributed mostly along the anisotropy axis (Figure S10). This length-dependent strain distribution explains the enhanced phase purity observed in longer HgTe NRs: more relaxed structures favor stabilization of the WZ phase. Such correlations between anisotropic shape of the NCs, lattice strain, and crystal phase are characteristic features of the elongated wurtzite NCs and have been reported to define the electronic properties of the anisotropic semi-

https://doi.org/10.1021/acsnano.6c01515
ACS Nano 2026, 20, 10686−10695

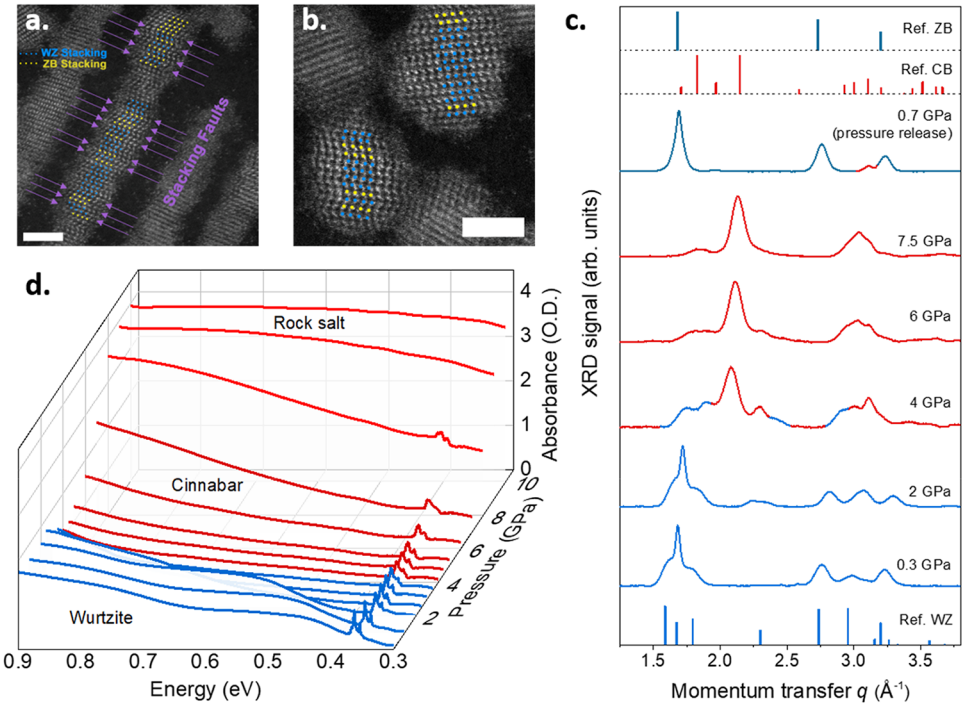

Figure 3. Stability of the WZ HgTe phase. (a) HR-STEM image of HgTe NR-55 showing the WZ (blue) and ZB (yellow) stacking sequence. The scale bar is 3 nm. (b) HR-STEM image of spherical HgTe NCs showing the stacking sequence between the WZ (blue) and ZB (yellow). The scale bar is 3 nm. The stacking sequence in panels (a) and (b) was identified starting from the top side toward the bottom of the images. (c) XRD patterns of HgTe NR-55 under different pressures; the pattern obtained once the pressure is released is also provided. Reference XRD patterns for each structure are shown as bars; WZ stands for wurtzite, CB is cinnabar, ZB is zinc blende. (d) Optical absorption spectra of HgTe NR-55 under different pressures. The spectral feature at 0.37 eV corresponds to ligand absorption. The color code of the spectra (blue for WZ and red for high-pressure crystal phases) matches the phase transitions shown in panel (c).

conductor systems.[34] It is worth noting that intermediate $Cu_{2-x}Te$ NCs are found to possess a hexagonal unit cell, further supporting a smooth phase transformation during cation exchange (Figure S11 and Table S3).

Changes in the diameter result in a noticeable redshift of the absorption feature of the initial CdTe NCs (Figure S12a). CdTe NCs display a band edge between 1.7 and 2 eV (Figure S12b), while the intermediate $Cu_{2-x}Te$ NCs exhibit a broad absorption band attributed to plasmonic scattering (Figure S12c), with features of both materials depending on their shape and size. In contrast, the negligible (<1 at. %) amount of Cu and Cd residuals ensures that the spectral tunability of HgTe NCs no longer results from a composition change, but is rather governed by the quantum confinement. The WZ HgTe NCs show a significantly reduced band gap in the 0.8−0.3 eV range and a corresponding redshift of the absorption edge (Figures 1f and S13a). This decrease in the band gap results from a combination of the intrinsic reduction of the bulk band gap and changes in the carrier effective mass affecting the confined energy levels. It is worth noting that the improved crystallinity of the HgTe NRs and strain relaxation along their anisotropy axis [001] led to a 2-fold reduction in the Urbach energy (Figure S13b,c). This energy describes the exponential decay of the density of states within the band gap, and thus the number of trap states, indicating that the WZ HgTe NRs possess sharper band edges compared to WZ spherical NCs, probably due to the specific lattice strain distribution.

Electronic Structure of WZ HgTe

After confirming the WZ crystal phase of the obtained spherical and elongated HgTe NCs, we focused on investigating their electronic structure. For that, we employed a combination of hard and soft X-ray photoemission (Figures 2a and S14) targeting the core levels relevant to the probed material, together with Raman spectroscopy to picture the low-energy excitation occurring in WZ HgTe. This combination of methods enables us to collect the excitation spectrum of the material over 5 orders of magnitude of energy and therefore capture all excitations without any pre-established assumption. For HgTe NR-30 with a 0.55 eV band gap, we found the Fermi level to be 0.3 eV above the top of the valence band, suggesting a quasi-intrinsic behavior with a slight *n*-type character as the Fermi level is localized in the upper half of the band gap. In turn, the Raman spectra show two main features at 15 meV (121 cm^{-1}) and 17.4 meV (140 cm^{-1}), which match well with the energies of the transverse and longitudinal optical phonons for ZB HgTe spherical NCs of a comparable diameter (Figure 2).[3] The features observed in the vibrational spectra of WZ and ZB HgTe NCs reflect the fact that the local environments of Hg and Te are very similar in these two atomic structures.

We then used density functional theory (DFT) with the HSE06 hybrid functional to assess the nature of the band gap of WZ HgTe. Specifically, because DFT is quite limited in terms of the system size to model the spectra of synthesized NRs, we applied a tight binding method, which is parametrized on the electronic structure determined from DFT-HSE06 (Tables S4 and S5, Figure S15). The electronic structure of bulk WZ HgTe is given in Figure 2d, while Figure 2c shows that of bulk ZB HgTe, for comparison. Similar to its ZB counterpart, bulk WZ HgTe does not show a gap, and is thus a semimetal. Remarkably, the conduction band crosses the valence band not at the Γ point, as in bulk ZB HgTe, but along

https://doi.org/10.1021/acsnano.6c01515
ACS Nano 2026, 20, 10686−10695

the k_z axis ($\Gamma-A$). The origin of this crossing results from the inversion of the s-p bands, which is also the origin of the topological properties of bulk ZB HgTe.[35] Note that each band at this crossing is twice degenerate along the $\Gamma-A$ direction, and thus, the crossover point has a degeneracy of 4, corresponding to a Dirac point. Consequently, our calculations predict that bulk WZ HgTe is a 3D Dirac semimetal without inversion symmetry, whose general properties have been discussed in ref 36. The degeneracy of the bands along the $\Gamma-A$ direction is explained by the symmetry of the point group $C6_v$, whose double group admits twice degenerate irreducible representations. This degeneracy is removed when we plot the dispersions along directions other than k_z from the Dirac point.

When considering WZ HgTe NCs, it is crucial to stress that the aforementioned effects impact a small energy range of the band structure, corresponding to a limited region of the Brillouin zone. Consequently, their influence will be negligible as long as confinement energies predominate (above around 200 meV, which corresponds to the experimental range of the band gap, 0.8−0.3 eV). It is also relevant to note that the band structure of WZ HgTe, obtained with the tight binding parameters of ZB HgTe, already shows good agreement with the DFT-HSE06 results (see Figure S15). This is due to the similarity of the chemical bonds between the ZB HgTe and WZ HgTe structures, as pointed out by the Raman spectrum in Figure 2b. We can, therefore, expect relatively similar confinement effects between these two crystalline forms of HgTe. Because of the semimetallic nature of WZ HgTe, the quantum confinement effect in the NCs makes it possible to vary their optical response from THz to mid-IR, similar to ZB HgTe NCs. In practice, the dispersion quickly deviates from a parabolic band and occurs in a linear regime. This is why a good agreement is obtained between the tight binding prediction and experimental data for the scaling of the band gap vs the inverse of the confined dimension, as shown in Figure 2e.

Pressure and Low-Temperature Stability of WZ HgTe NCs

We then investigated the stability of the WZ HgTe phase. Consistent with XRD data, high-resolution scanning transmission electron microscopy (HR-STEM) images (Figure 3a,b) revealed that the obtained WZ HgTe NCs are in fact not pure in terms of the crystal phase: a single nanocrystal is rather composed of successive segments of ZB and WZ phases, though the latter one prevails. Similar behavior has been reported for the III−V nanowires[37] and Cd chalcogenide NCs,[38] and strongly depends on the ligand-assisted surface chemistry.[39] This combination of phases and associated interfaces is certainly at the origin of the lattice strains and may be involved in the stabilization of the metastable WZ phase of HgTe, as well as govern the electronic properties of the material.

To shed light on the stability of the WZ HgTe phase, we performed pressure-dependent studies in a diamond anvil cell probing both structural changes and infrared absorption of HgTe NCs; Figure S16 explains the details of the experimental setups. Methanol/ethanol mixture and NaCl were used as pressure-transmitting media to ensure quasi-hydrostatic conditions up to 10 GPa. Upon pressure application, XRD patterns of HgTe NR-55 shifted toward larger wavevector values, consistent with a compressed lattice (Figures 3c, S17, and S18). Between 3 and 4 GPa, the reflections assigned to the cinnabar (CB) phase of HgTe emerged in the XRD pattern. This phase transition matches the one of bulk ZB HgTe reported in the literature,[17,29,40,41] but with thresholds that are shifted toward higher pressure, since in bulk, the ZB-to-CB transformation happens at 1.4 GPa. For ZB HgTe NCs, the phase changes are reversible, though hysteretic: the threshold pressures are different in up and down sweeps. Remarkably, the situation is different for WZ HgTe NCs, where the peak at 1.7 $Å^{-1}$ becomes narrower, while the peak at 3 $Å^{-1}$ is suppressed. Mostly, after the release of pressure, the XRD patterns of NR-55 and spherical NCs match the ZB phase (with [111] anisotropy axis for NRs), highlighting the metastable character of the WZ HgTe (Figures 3c and S17).

The sequence of these structural phase transformations is also accompanied by changes in the electronic properties, namely, the massive shift of the IR absorption spectra under various pressures (Figure 3d). Upon increasing the pressure, the band edge of the compressed WZ HgTe NR-55 experiences blueshift. Simultaneously, its IR absorption becomes very weak after the transition to the CB phase (which happens from 4 to 7 GPa), consistent with the wider band gap of this crystal phase.[41] Finally, when the rock salt phase of HgTe is attained above 7 GPa, absorbance appears to increase within the studied spectral range. This phase is expected to be metallic, and therefore the sample becomes reflecting, reducing the transmitted signal,[2,29,30,40] which appears as an increased absorption in Figure 3d. The same trends are observed for the WZ HgTe NRs of shorter lengths as well as for spherical WZ NCs (Figure S19). Notably, the shape of the IR absorption spectrum with well-defined excitonic features is recovered (Figure S20) when the pressure is released, despite the loss of the metastable WZ phase, due to the similarity of the electronic structure of the two phases (ZB and WZ) when the confinement exceeds 200 meV.

The nonzero band gap makes the WZ phase of HgTe NCs appealing for IR optoelectronic devices, which often operate under cryogenic conditions. Therefore, the optical properties of the material were explored under cooling down to 10 K. Once the material is brought to a low temperature (see Figure S21), a redshift of the absorbance spectrum is observed, with a value of dE_g/dT in the 200−300 $\mu eV \cdot K^{-1}$ range depending on the NR dimensions. Larger NRs with a reduced quantum confinement show a larger redshift. This behavior matches the one observed for the ZB HgTe spherical NCs, which also exhibited a redshift upon cooling down to the same temperatures.[2,30,42]

Electroluminescence above 2 μm from WZ HgTe NRs

Finally, we tested the potential of the WZ HgTe NCs for IR optoelectronics through their integration into a light-emitting diode (LED). In the short-wave IR spectral range and up to 1.7 μm, lots of efforts have been dedicated to demonstrating LEDs based on PbS[43,44] and III−V[45] semiconductor NCs. The key advantage of HgTe NCs is their ability to emit photons at even longer wavelengths than the aforementioned materials. Indeed, WZ HgTe NCs not only exhibit well-defined excitonic features in the range from 1 to 0.4 eV (Figure 1f), but also size-tunable IR photoluminescence (PL), as shown in Figure S22. Importantly, the PL quantum yield of the WZ HgTe NRs is substantially higher than that of the WZ spherical NCs (Figures S23 and S24), reaching 20% at 2 μm for the shortest NR-20 in solution compared to 3% for spherical NCs (Table S6). We assume this difference arises from the reduced lattice strains and anisotropic geometry of the NRs, which leads to

https://doi.org/10.1021/acsnano.6c01515
ACS Nano 2026, 20, 10686−10695

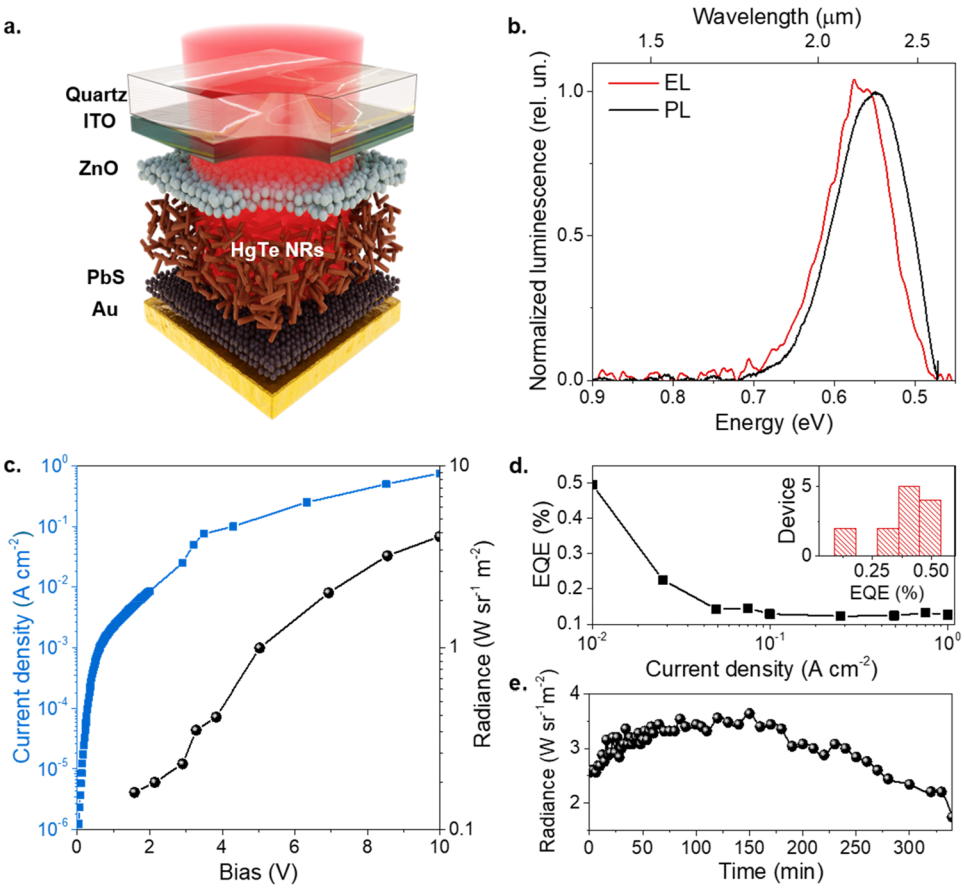

Figure 4. Short-wave IR electroluminescence from the LED based on WZ HgTe NR-20. (a) Schematics of the LED structure consisting of a quartz substrate, ITO as the cathode, ZnO as the electron transport layer, HgTe NRs-20 blended with ZnO NCs (1:1 = v:v) as a light-emitting layer, thiol-treated PbS NCs as a hole transport layer, and Au as the anode. (b) Normalized PL and EL spectra. The EL spectrum was measured under 5 V bias voltage, while the PL spectrum was recorded from the same LED under zero bias voltage and 780 nm laser excitation. (c) Current density and radiance of the LED as functions of the applied bias voltage. (d) EQE of the LED as a function of the driving current. The inset shows the statistics of the peak EQE taking into account 13 devices. (e) Radiance of the LED as a function of time under constant bias voltage of 8 V.

different packing arrangements in films and helps to preserve higher emission efficiency in the solid state. Additionally, the elongated shape of NRs results in a reduced NC-NC contact area per unit volume in close-packed films, which limits nonradiative energy transfer pathways between adjacent NCs. The PL quantum yield expectably decreases to 2.4% when the NRs are deposited as a film on a sapphire substrate, yet it remains among the highest values reported for this spectral range.[8]

Thus, we used WZ HgTe NR-20 to fabricate the LED, with the design inspired by previous studies on IR-emitting II−VI NCs,[46,47] with ZnO and PbS NC layers used respectively as electron and hole injector. A schematic of the device is shown in Figure 4a, while the band alignment of the constituent layers is provided in Figure S25. We note that the blending of light-emitting NRs with ZnO NCs leads to less pronounced hysteresis and more stable LED operation (Figure S26).[46,48] The electroluminescence (EL) spectrum of the LED largely overlaps with the PL spectrum of NR-20 measured from the same, unbiased device, although the EL peak is shifted to higher energy (Figure 4b). Importantly, this feature is reproducible and does not depend on the instrumentation or sample type (Figure S27). We postulate that the observed mismatch between the PL and EL maxima arises from several factors. First, PL in II−VI NCs can originate from both a band-edge transition and radiative recombination via lower-energy in-gap states. Such trap states are a prominent feature of semiconductor NCs capped with Z-type ligands such as mercury thiolates, and their contribution increases as these ligands are removed from the NC surface.[49] The ratio of trap-related emission in the PL band, and thus the magnitude of the PL redshift, depends on the excitation conditions and trap concentration, which may be higher in NRs due to a larger surface-to-volume ratio compared to spherical NCs. On the other hand, trap-assisted radiative recombination also contributes to the EL, but its impact is not yet fully developed and does not dominate at the early stage of the LED lifetime (<20 min, i.e., within the time scale of our EL experiment). Furthermore, it has been shown that under high driving bias, the EL maximum may experience a blueshift due to an elevated electronic temperature relative to the lattice (phonon) temperature, indicating nonequilibrium device operation.[50] Taken together, those factors lead to the mismatch between the PL and EL maxima.

The radiance of the device reaches 5 $W \cdot Sr^{-1} \cdot m^{-2}$ (Figure 4c), which exceeds the value reported for ZB HgTe NCs-based LED,[48] while the driving current is two orders of magnitude lower than in that previous work. This indicates a higher external quantum efficiency (EQE) of the WZ HgTe NR-20-based LED, which indeed reaches the value of 0.5% (Figure

https://doi.org/10.1021/acsnano.6c01515
ACS Nano 2026, 20, 10686−10695

4d), compared with a maximum of 0.25 % for LEDs based on ZB HgTe spherical NCs operating at the same wavelength (2.2 μm).[48] Despite the simple device architecture, the obtained EQE and radiance are, the highest achieved beyond 2 μm at non-cryogenic temperature from colloidal material (see Table S7 and Figure S25−27). Nevertheless, the turn-on voltage for the LED (1.5 V) remains higher than the bandgap of WZ HgTe NRs-20 (0.67 eV), and the operational stability is only moderate over time (Figure 4e), indicating that further optimization of the device structure and the HgTe NR doping to improve charge injection will be required to push the performance further.

CONCLUSIONS

To summarize, we synthesized a series of WZ HgTe NCs (both elongated and spherical ones) with band edge energies spanning from 0.8 to 0.3 eV, which makes them highly appealing for a variety of applications in the short- to mid-wave IR ranges. Our DFT and tight binding calculations show that bulk WZ HgTe is a semimetal and, in contrast to the ZB structure, the Dirac point is not localized at the center of the Brillouin zone. Away from the Γ point, under quantum confinement, the optical and vibrational properties of WZ HgTe NCs (optical band gap scaling with diameter and phonon spectrum) appear very similar to what has been observed for the ZB phase of HgTe NCs. The metastable nature of the WZ HgTe phase was confirmed by conducting structural and optical investigations under pressure, which leads to an irreversible transformation from WZ to ZB once pressure is released. Taking advantage of the high PL quantum yield of the WZ HgTe NRs, we integrated them into an LED to reach the wavelength range beyond 2 μm where obtaining detectable EL is challenging. The LEDs based on WZ HgTe NRs are twice as efficient as those based on ZB HgTe NCs reported previously.

METHODS

Ligand Exchange on CdTe NCs

In a glovebox, 1 mL of CdTe NC solution in toluene (20 mg/mL) was diluted with 1 mL of toluene and added to 1 mL of DDT and 100 μL of OlAm. The mixture was heated to 60 °C and stirred overnight. After that, the CdTe NCs were precipitated with ethanol, centrifuged, redispersed in 1 mL of toluene, precipitated with ethanol, and finally redispersed in 2 mL of toluene.

Cd-to-Cu Exchange in a Nonpolar Solvent Mixture

In a glovebox, 2 mL of CdTe NCs (10 mg/mL) capped with DDT ligands were added to 2.5 mL of 0.1 M Cu-Oleate solution and stirred for 5 min. Then, methanol was added to the mixture to precipitate the $Cu_{2-x}Te$ NCs; the mixture was centrifuged, and the precipitate was redispersed in 4 mL of outgassed chloroform and kept in the glovebox.

Cu-to-Hg Cation Exchange with Hg-Thiolate

In a glovebox, 4 mL of chloroform solution of $Cu_{2-x}Te$ NCs was added to 4 mL of chloroform solution containing 175.5 mg of Hg-thiolate precursor, followed by the addition of 240 μL of TOP and 30 μL of DDT. The mixture was stirred for 2 h, and the obtained HgTe NCs were precipitated by ethanol, redispersed in 1 mL of chloroform, and precipitated by ethanol again. Finally, NCs were redispersed either in hexane for the ligand exchange or in TCE for optical measurements.

X-ray Diffraction under Pressure

X-ray powder diffraction measurements were carried out at the XRD platform of the IMPMC on a Rigaku MM007HF diffractometer equipped with a Mo rotating anode ($\lambda_{K\alpha1}$ = 0.709319 Å, $\lambda_{K\alpha2}$ = 0.713609 Å), Varimax focusing optics, and a RAXIS4++ image plate detector. X-ray data were collected at 20 °C. A LaB_6 standard sample was measured under the same experimental conditions to calibrate the Fit2D program, the image processing software used to integrate the intensities around the Debye−Scherrer rings and to get the 1D patterns.

Infrared Absorption Spectra under Pressure

IR absorption measurements were performed at the SMIS beamline of synchrotron SOLEIL, using a horizontal microscope equipped with two custom Schwarzschild objectives (NA = 0.5), which allow focusing inside the diamond anvil cells. The microscope was used in transmission configuration and coupled to a Thermo Fisher Nicolet iS50 FTIR spectrometer with synchrotron light as IR source, a KBr beamsplitter, and a MCT detector to acquire spectra with 100 scans and a spectral resolution of 4 cm^{-1}.

Infrared LED Characterization

The fabrication of the LED, whose structure was inspired by refs 46,48, is described in detail in the Supporting Information. All LED characterizations were performed in the air with no encapsulation and at room temperature. Assuming that the LED emission is Lambertian, the flux leaving the device directly can be described as $P = \int_0^{\pi/2} 2\pi L_0 \cos\theta \sin\theta \, d\theta = \pi L_0$, where L_0 is the flux per solid angle of light leaving the device in the forward direction. The number of photons emitted per second to the forward direction was obtained by $N_P = \frac{P}{h\nu} = \frac{\lambda P}{hc}$, with λ the wavelength of the electroluminescence peak, h the Planck's constant, and c the speed of light. The number of electrons injected per second can be obtained by $N_e = \frac{I}{e}$, with I the current flow in the device. Thus, the EQE can be calculated as $EQE = \frac{N_P}{N_e} = \frac{\lambda e P}{hcI}$, and the radiance of the device $R = \frac{L_0}{s_2} = \frac{P}{\pi s_2}$, with S_2 the area of the LED pixel.

The emitted optical power was measured using an extended InGaAs sensor (Thorlabs DET10D2, pixel size 0.8 mm^2) that has a 2.6 μm cut-off wavelength. A pair of IR-transparent lenses and a gold parabolic mirror were used to focus the emission from the fabricated LEDs to the small area of the InGaAs sensor. A Keithley 2400 instrument was used to apply the driving bias voltage and measure the current flowing through the fabricated LEDs.

For the electroluminescence, the LED was powered with a signal generator at 5 V bias and a pulsing frequency of 10 kHz. The modulated light was focused by a gold parabolic mirror into the input of an FTIR spectrometer (Thermo Fisher IS 50R) in a step scan regime. In the instrument, the emission from the LED went through the CaF_2 beamsplitter and was collected by an extended InGaAs or DTGS detector. The output of the detector was fed into a lock-in amplifier (SR510 Stanford Research System) that was synchronized with the signal generator. The output signal was reinjected into the FTIR instrument to operate in step scan mode.

ASSOCIATED CONTENT

Supporting Information

The Supporting Information is available free of charge at https://pubs.acs.org/doi/10.1021/acsnano.6c01515.

Evidence for the Cd and Cu impurities removal from the WZ HgTe NCs during the cation exchange, morphology and crystal structure of the WZ HgTe NCs under ambient conditions, optical absorption and band gap of WZ HgTe NCs, electronic structure of WZ HgTe NCs derived by XPS, electronic structure modeling of bulk WZ HgTe, pressure stability of WZ HgTe NCs, temperature stability of the WZ HgTe NCs, PL efficiency, and characterization of short-wavelength IR LED based on WZ HgTe NRs (PDF)

https://doi.org/10.1021/acsnano.6c01515
ACS Nano 2026, 20, 10686−10695

AUTHOR INFORMATION

Corresponding Authors

Andrey L. Rogach − *Department of Materials Science and Engineering, City University of Hong Kong, Hong Kong S.A.R. 999077, P. R. China;* orcid.org/0000-0002-8263-8141; Email: andrey.rogach@cityu.edu.hk

Emmanuel Lhuillier − *Sorbonne Université, CNRS, Institut des NanoSciences de Paris, Paris 75005, France;* orcid.org/0000-0003-2582-1422; Email: el@insp.upmc.fr

Authors

Kseniia A. Sergeeva − *Department of Materials Science and Engineering, City University of Hong Kong, Hong Kong S.A.R. 999077, P. R. China*

Arsenii S. Portniagin − *Department of Materials Science and Engineering, City University of Hong Kong, Hong Kong S.A.R. 999077, P. R. China*

Dario Mastrippolito − *Sorbonne Université, CNRS, Institut des NanoSciences de Paris, Paris 75005, France;* orcid.org/0000-0001-6360-7254

Clement Gureghian − *Sorbonne Université, CNRS, Institut des NanoSciences de Paris, Paris 75005, France*

Antoine Hage − *Université Lille, CNRS, Univ. Polytechnique Hauts-de-France, Lille 59000, France*

Dries De Pesseroey − *Sorbonne Université, CNRS, Institut des NanoSciences de Paris, Paris 75005, France;* orcid.org/0009-0005-8306-5401

Marco Paye − *Sorbonne Université, CNRS, Institut des NanoSciences de Paris, Paris 75005, France*

Erwan Bossavit − *Sorbonne Université, CNRS, Institut des NanoSciences de Paris, Paris 75005, France; Synchrotron SOLEIL, L'Orme des Merisiers, Saint-Aubin 91190, France;* orcid.org/0000-0001-6088-3309

Aleksandr A. Sergeev − *Department of Physics, Hong Kong University of Science and Technology, Hong Kong S.A.R. 999077, P. R. China*

Zhuo Li − *Department of Materials Science and Engineering, City University of Hong Kong, Hong Kong S.A.R. 999077, P. R. China*

Albin Colle − *Sorbonne Université, CNRS, Institut des NanoSciences de Paris, Paris 75005, France*

Céline Rivaux − *Université Grenoble Alpes, CEA, CNRS, IRIG, SyMMES, Grenoble 38000, France*

Sandrine Ithurria − *Laboratoire de Physique et d'Etude des Matériaux, ESPCI, PSL Research University, Sorbonne Université, CNRS, Paris 75005, France;* orcid.org/0000-0002-4733-9883

Peter Reiss − *Université Grenoble Alpes, CEA, CNRS, IRIG, SyMMES, Grenoble 38000, France;* orcid.org/0000-0002-9563-238X

Gilles Patriarche − *Centre de Nanosciences et de Nanotechnologies, CNRS, Université Paris-Saclay, Palaiseau 92110, France;* orcid.org/0000-0002-3917-2470

Xiaoyan Zhong − *Department of Materials Science and Engineering, City University of Hong Kong, Hong Kong S.A.R. 999077, P. R. China;* orcid.org/0000-0001-8990-2198

Jing Li − *Université Grenoble Alpes, CEA, Leti, Grenoble 38000, France*

Stefan Klotz − *Sorbonne Université, Muséum National d'Histoire Naturelle, CNRS, Institut de Minéralogie, de Physique des Matériaux et de Cosmochimie, Paris 75005, France*

Benoit Baptiste − *Sorbonne Université, Muséum National d'Histoire Naturelle, CNRS, Institut de Minéralogie, de Physique des Matériaux et de Cosmochimie, Paris 75005, France*

Debora Pierucci − *Sorbonne Université, CNRS, Institut des NanoSciences de Paris, Paris 75005, France;* orcid.org/0000-0001-8751-1994

Francesco Capitani − *Synchrotron SOLEIL, L'Orme des Merisiers, Saint-Aubin 91190, France;* orcid.org/0000-0003-1161-7455

Christophe Delerue − *Université Lille, CNRS, Univ. Polytechnique Hauts-de-France, Lille 59000, France;* orcid.org/0000-0002-0427-3001

Complete contact information is available at: https://pubs.acs.org/10.1021/acsnano.6c01515

Author Contributions

[††]K.A.S. and A.S.P. contributed equally to this work. K.A.S., A.S.P., A.L.R., and E.L. germinated the project. A.L.R., E.L., C.D., P.R., and S.I. funded the project. A.S.P. developed a synthesis procedure for wurtzite HgTe nanocrystals and performed their composition characterization. A.S.P., Z.L., X.Z., and G.P. performed TEM studies. K.A.S. and A.A.S. performed infrared optical characterization. K.A.S., B.B., and S.K. performed XRD measurements under pressure. K.A.S., M.P., D.D.P., C.G., and F.C. performed IR measurements under pressure. K.A.S. performed IR measurements at low temperature. K.A.S. and E.B. fabricated and characterized the LEDs. Other colloidal materials used in this study have been produced by C.R., P.R., S.I., and A.C. D.M. and D.P. acquired the Raman and XPS spectra. J.L., A.H., and C.D. conducted electronic structure modeling. K.A.S., A.S.P., A.L.R., and E.L. wrote and revised the manuscript. All authors read, corrected, and approved the content.

Funding

This study was supported by the ERC grant AQDtive (grant no. 101086358) and by the French National Research Agency (ANR) through the grants Quicktera (ANR-22-CE09−0018), Operatwist (ANR-22-CE09−0037−01), E-map (ANR-23-CE50−0025), DIRAC (ANR-24-ASM1−0001), camIR (ANR-24-CE42−2757), Piquant (ANR-24-CE09−0786), Phasecraft (ANR-25-CE08−5762−02), and nanomirage (ANR-25-CE09−3398). The study was also supported by the Innovation and Technology Commission of Hong Kong (ITS/027/22MX) and the Research Grant Council of Hong Kong SAR through the RGC Senior Research Fellow Scheme (SRFS 2324−1S04). We acknowledge the use of clean-room facilities at the "Centrale de Proximité Paris-Centre" and support from Renatech+ for micro- and nanofabrication, and the financial support from the CNRS through the MITI interdisciplinary programs (project WITHIN) and Region Ile de France through the Sesame project INSIDE. Z.L. and X.Y.Z. acknowledge the financial support from NSFC (52171014), GuangDong Basic and Applied Basic Research Foundation (2024A1515012303), Sino-German Center for Research Promotion (M-0265), RGC (E-CityU101/20), and European Research Council (856538, "3D MAGiC").

Notes

The authors declare no competing financial interest.

https://doi.org/10.1021/acsnano.6c01515
ACS Nano 2026, 20, 10686−10695

REFERENCES

(1) Izquierdo, E.; Robin, A.; Keuleyan, S.; et al. Strongly Confined HgTe 2D Nanoplatelets as Narrow Near-Infrared Emitters. *J. Am. Chem. Soc.* **2016**, *138*, 10496−10501.

(2) Moghaddam, N.; Gréboval, C.; Qu, J.; et al. The Strong Confinement Regime in HgTe Two-Dimensional Nanoplatelets. *J. Phys. Chem. C* **2020**, *124*, 23460−23468.

(3) Goubet, N.; Jagtap, A.; Livache, C.; et al. Terahertz HgTe Nanocrystals: Beyond Confinement. *J. Am. Chem. Soc.* **2018**, *140*, 5033−5036.

(4) Dornhaus, R.; Nimtz, G. The Properties and Applications of the Hg1−xCdxTe Alloy System. In *Narrow-Gap Semiconductors*; Dornhaus, R.; Nimtz, G.; Schlicht, B., Eds.; Springer Berlin Heidelberg: Berlin, Heidelberg, 1983; pp 119−281 .

(5) Man, P.; Pan, D. S. Infrared absorption in HgTe. *Phys. Rev. B* **1991**, *44*, No. 8745.

(6) Orlowski, N.; Augustin, J.; Gołacki, Z.; Janowitz, C.; Manzke, R. Direct evidence for the inverted band structure of HgTe. *Phys. Rev. B* **2000**, *61*, No. R5058.

(7) Svane, A.; Christensen, N. E.; Cardona, M.; et al. Quasiparticle band structures of β-HgS, HgSe, and HgTe. *Phys. Rev. B* **2011**, *84*, No. 205205.

(8) Sergeeva, K. A.; Zhang, H.; Portniagin, A. S.; et al. The Rise of HgTe Colloidal Quantum Dots for Infrared Optoelectronics. *Adv. Funct. Mater.* **2024**, *34*, No. 2405307.

(9) Rogalski, A. HgCdTe infrared detector material: history, status and outlook. *Rep. Prog. Phys.* **2005**, *68*, No. 2267.

(10) Lei, W.; Antoszewski, J.; Faraone, L. Progress, challenges, and opportunities for HgCdTe infrared materials and detectors. *Appl. Phys. Rev.* **2015**, *2*, No. 041303.

(11) Lhuillier, E.; Dang, T. H.; Cavallo, M.et al. Electronic Structure of Mercury Chalcogenides Nanocrystals. In *Handbook of II-VI Semiconductor-Based Sensors and Radiation Detectors*; Springer International Publishing: Cham, 2023; pp 133−156 .

(12) Keuleyan, S. E.; Guyot-Sionnest, P.; Delerue, C.; Allan, G. Mercury telluride colloidal quantum dots: Electronic structure, size-dependent spectra, and photocurrent detection up to 12 μm. *ACS Nano* **2014**, *8*, 8676−8682.

(13) Climente, J. I.; Szafran, B. Electronic Structure and Optical Spectrum of Thick HgTe Colloidal Nanoplatelets. *ACS Photonics* **2023**, *10*, 3763−3771.

(14) Allan, G.; Delerue, C. Tight-binding calculations of the optical properties of HgTe nanocrystals. *Phys. Rev. B* **2012**, *86*, No. 165437.

(15) König, M.; Wiedmann, S.; Brüne, C.; et al. Quantum Spin Hall Insulator State in HgTe Quantum Wells. *Science* **2007**, *318*, 766−770.

(16) Beugeling, W.; Kalesaki, E.; Delerue, C.; et al. Topological states in multi-orbital HgTe honeycomb lattices. *Nat. Commun.* **2015**, *6*, No. 6316.

(17) San-Miguel, A.; Wright, N. G.; McMahon, M. I.; Nelmes, R. J. Pressure evolution of the cinnabar phase of HgTe. *Phys. Rev. B* **1995**, *51*, No. 8731.

(18) Mahler, B.; Lequeux, N.; Dubertret, B. Ligand-Controlled Polytypism of Thick-Shell CdSe/CdS Nanocrystals. *J. Am. Chem. Soc.* **2010**, *132*, 953−959.

(19) Sun, H.; Buhro, W. E. Contrasting Ligand-Exchange Behavior of Wurtzite and Zinc-Blende Cadmium Telluride Nanoplatelets. *Chem. Mater.* **2021**, *33*, 1683−1697.

(20) Yu, W. W.; Wang, Y. A.; Peng, X. Formation and Stability of Size-, Shape-, and Structure-Controlled CdTe Nanocrystals: Ligand Effects on Monomers and Nanocrystals. *Chem. Mater.* **2003**, *15*, 4300−4308.

(21) Aubert, T.; Golovatenko, A. A.; Samoli, M.; et al. General Expression for the Size-Dependent Optical Properties of Quantum Dots. *Nano Lett.* **2022**, *22*, 1778−1785.

(22) Abbassi, A.; Zarhri, Z.; Azahaf, C.; Ez-Zahraouy, H.; Benyoussef, A. Boltzmann equations and ab initio calculations: comparative study of cubic and wurtzite CdSe. *SpringerPlus* **2015**, *4*, No. 543.

(23) Efros, A. L.; Rosen, M.; Kuno, M.; et al. Band-edge exciton in quantum dots of semiconductors with a degenerate valence band: Dark and bright exciton states. *Phys. Rev. B* **1996**, *54*, No. 4843.

(24) Manna, L.; Scher, E. C.; Alivisatos, A. P. Synthesis of Soluble and Processable Rod-, Arrow-, Teardrop-, and Tetrapod-Shaped CdSe Nanocrystals. *J. Am. Chem. Soc.* **2000**, *122*, 12700−12706.

(25) Peng, X.; Manna, L.; Yang, W.; et al. Shape control of CdSe nanocrystals. *Nature* **2000**, *404*, 59−61.

(26) Ithurria, S.; Tessier, M. D.; Mahler, B.; et al. Colloidal nanoplatelets with two-dimensional electronic structure. *Nat. Mater.* **2011**, *10*, 936−941.

(27) Diroll, B. T.; Guzelturk, B.; Po, H.; et al. 2D II−VI Semiconductor Nanoplatelets: From Material Synthesis to Optoelectronic Integration. *Chem. Rev.* **2023**, *123*, 3543−3624.

(28) Portniagin, A. S.; Sergeeva, K. A.; Kershaw, S. V.; Rogach, A. L. Cation-Exchange-Derived Wurtzite HgTe Nanorods for Sensitive Photodetection in the Short-Wavelength Infrared Range. *Chem. Mater.* **2023**, *35*, 5631−5639.

(29) McMahon, M. I.; Wright, N. G.; Allan, D. R.; Nelmes, R. J. High-pressure crystal structure of HgTe-IV. *Phys. Rev. B* **1996**, *53*, No. 2163.

(30) Livache, C.; Goubet, N.; Gréboval, C.; et al. Effect of Pressure on Interband and Intraband Transition of Mercury Chalcogenide Quantum Dots. *J. Phys. Chem. C* **2019**, *123*, 13122−13130.

(31) Izquierdo, E.; Dufour, M.; Chu, A.; et al. Coupled HgSe Colloidal Quantum Wells through a Tunable Barrier: A Strategy to Uncouple Optical and Transport Band Gap. *Chem. Mater.* **2018**, *30*, 4065−4072.

(32) Gupta, S.; Kershaw, S. V.; Susha, A. S.; et al. Near-Infrared-Emitting CdxHg1−xSe Nanorods Fabricated by Ion Exchange in an Aqueous Medium. *ChemPhysChem* **2013**, *14*, 2853−2858.

(33) Portniagin, A. S.; Sergeev, A. A.; Sergeeva, K. A.; et al. Removing Cadmium Impurities from Cation-Exchange-Derived CuInSe2/CuInS2 Nanorods for Enhanced Infrared Emission and Photodetection. *Adv. Funct. Mater.* **2024**, *34*, No. 2400942.

(34) Shulenberger, K. E.; Jilek, M. R.; Sherman, S. J.; Hohman, B. T.; Dukovic, G. Electronic Structure and Excited State Dynamics of Cadmium Chalcogenide Nanorods. *Chem. Rev.* **2023**, *123*, 3852−3903.

(35) Bernevig, B. A.; Hughes, T. L.; Zhang, S.-C. Quantum Spin Hall Effect and Topological Phase Transition in HgTe Quantum Wells. *Science* **2006**, *314*, 1757−1761.

(36) Gao, H.; Strockoz, J.; Frakulla, M.; Venderbos, J. W. F.; Weng, H. Noncentrosymmetric topological Dirac semimetals in three dimensions. *Phys. Rev. B* **2021**, *103*, No. 205151.

(37) Glas, F.; Harmand, J.-C.; Patriarche, G. Why Does Wurtzite Form in Nanowires of III-V Zinc Blende Semiconductors? *Phys. Rev. Lett.* **2007**, *99*, No. 146101.

(38) Saruyama, M.; So, Y. G.; Kimoto, K.; et al. Spontaneous Formation of Wurzite-CdS/Zinc Blende-CdTe Heterodimers through a Partial Anion Exchange Reaction. *J. Am. Chem. Soc.* **2011**, *133*, 17598−17601.

(39) Xiao, T.; Nagaoka, Y.; Wang, X.; et al. Nanocrystals with metastable high-pressure phases under ambient conditions. *Science* **2022**, *377* (1979), 870−874.

(40) Werner, A.; Hochheimer, H. D.; Strossner, K.; Jayaraman, A. High-pressure x-ray diffraction studies on Hg Te and Hgs to 20 GPa. *Phys. Rev. B* **1983**, *28*, No. 3330.

(41) Wright, N. G.; McMahon, M. I.; Nelmes, R. J.; San-Miguel, A. Crystal structure of the cinnabar phase of HgTe. *Phys. Rev. B* **1993**, *48*, No. 13111.

(42) Lhuillier, E.; Keuleyan, S.; Guyot-Sionnest, P. Erratum: Optical properties of HgTe colloidal quantum dots. *Nanotechnology* **2014**, *25*, No. 189501.

(43) Tessler, N.; Medvedev, V.; Kazes, M.; Kan, S.; Banin, U. Efficient Near-Infrared Polymer Nanocrystal Light-Emitting Diodes. *Science* **2002**, *295*, 1506−1508.

(44) Pradhan, S.; Dalmases, M.; Taghipour, N.; Kundu, B.; Konstantatos, G. Colloidal Quantum Dot Light Emitting Diodes at

https://doi.org/10.1021/acsnano.6c01515
ACS Nano 2026, 20, 10686−10695

Telecom Wavelength with 18% Quantum Efficiency and Over 1 MHz Bandwidth. *Adv. Sci.* **2022**, *9*, No. 2200637.
(45) Zhao, X.; Lim, L. J.; Ang, S. S.; Tan, Z.-K. Efficient Short-Wave Infrared Light-Emitting Diodes Based on Heavy-Metal-Free Quantum Dots. *Adv. Mater.* **2022**, *34*, No. 2206409.
(46) Pradhan, S.; Di Stasio, F.; Bi, Y.; et al. High-efficiency colloidal quantum dot infrared light-emitting diodes via engineering at the supra-nanocrystalline level. *Nat. Nanotechnol* **2019**, *14*, 72−79.
(47) Qu, J.; Rastogi, P.; Gréboval, C.; et al. Electroluminescence from HgTe Nanocrystals and Its Use for Active Imaging. *Nano Lett.* **2020**, *20*, 6185−6190.
(48) Qu, J.; Weis, M.; Izquierdo, E.; et al. Electroluminescence from nanocrystals above 2 μm. *Nat. Photonics* **2022**, *16*, 38−44.
(49) Geiregat, P.; Houtepen, A. J.; Sagar, L. K.; et al. Continuous-wave infrared optical gain and amplified spontaneous emission at ultralow threshold by colloidal HgTe quantum dots. *Nat. Mater.* **2018**, *17*, 35−41.
(50) Bossavit, E.; Qu, J.; Abadie, C.; et al. Optimized Infrared LED and Its Use in an All-HgTe Nanocrystal-Based Active Imaging Setup. *Adv. Opt. Mater.* **2022**, *10*, No. 2101755.

https://doi.org/10.1021/acsnano.6c01515
ACS Nano 2026, 20, 10686−10695